Photonic indistinguishability of the tin-vacancy center in nanostructured diamond

Jesús Arjona Martínez[1,*], Ryan A. Parker[1,*], Kevin C. Chen[2], Carola M. Purser[1], Linsen Li[2], Cathryn P. Michaels[1], Alexander M. Stramma[1], Romain Debroux[1], Isaac B. Harris[2], Martin Hayhurst Appel[1], Eleanor C. Nichols[1], Matthew E. Trusheim[2], Dorian A. Gangloff[1,3,†], Dirk Englund[2,†], and Mete Atatüre[1,†]

[1] *Cavendish Laboratory, University of Cambridge, JJ Thomson Avenue, Cambridge CB3 0HE, United Kingdom*

[2] *Department of Electrical Engineering and Computer Science, Massachusetts Institute of Technology, Cambridge, Massachusetts 02139, USA and*

[3] *Department of Engineering Science, University of Oxford, Parks Road, Oxford, OX1 3PJ*

(Dated: December 7, 2022)

Tin-vacancy centers in diamond are promising spin-photon interfaces owing to their high quantum-efficiency, large Debye-Waller factor, and compatibility with photonic nanostructuring. Benchmarking their single-photon indistinguishability is a key challenge for future applications. Here, we report the generation of single photons with $99.7^{+0.3}_{-2.5}$% purity and 63(9)% indistinguishability from a resonantly excited tin-vacancy center in a single-mode waveguide. We obtain quantum control of the optical transition with 1.71(1)-ns-long π-pulses of 77.1(8)% fidelity. A modest Purcell enhancement factor of 12 would enhance the indistinguishability to 95%. The greater than 100 ms spectral stability shown would then enable strings of up to 10^6 identical photons to be generated.

Indistinguishable photons from quantum emitters provide a fundamental resource for scalable quantum communication and have been employed to realize linear optical quantum computation [1–3], spin-photon and spin-spin entanglement [4–6], and quantum repeater schemes [7–10]. Experimentally, the photonic indistinguishability can be benchmarked through two-photon quantum interference known as the Hong-Ou-Mandel (HOM) effect. The HOM indistinguishability places a bound on the fidelities achievable in photon-mediated gates and entanglement distribution in measurement-based protocols [11–13]. This effect has been observed across multiple solid-state emitters such as the nitrogen-, silicon- and germanium-vacancies in diamond [14–16], defects in silicon-carbide [17], and semiconductor quantum dots [18].

Within solid-state emitters, the negatively charged group-IV centers in diamond stand as promising spin-photon interfaces due to their large Debye-Waller factor (60% - 80%) [19–22], competitive quantum efficiency (10% - 80%) [21–24] and first-order insensitivity to electric-field noise [25, 26]. This electric-field agnosticism makes them inherently compatible with complex photonic nanostructuring, as the disordered charge environment present at the diamond interface does not couple deleteriously to a proximate emitter. Accordingly, high collection efficiency [27, 28], Purcell enhanced emission [29, 30], and incorporation into photonic integrated circuits [31] have been demonstrated using group-IV centers embedded in diamond. The negatively charged tin-vacancy (SnV) is particularly promising. Its large ground-state orbital splitting inhibits phonon-mediated dephasing [32], allowing for operation at a temperature accessible in standard helium closed-cycle cryostats. Accordingly, a spin-coherence time (T_2) of 0.30(8) ms at 1.7 K has been achieved using a SnV center [33]; longer than that of other group-IV emitters at this temperature. Observation of transform-limited emission in bulk diamond [34] and advancements in fabrication and charge stability [35] further demonstrate that SnV centers are a suitable spin-photon interface for quantum networking and measurement-based computation protocols [12]. Probing the optical coherence of the emitted photons is the only major unexplored benchmark for this spin-photon interface.

In this work, we report the observation of quantum interference of single photons from a SnV center in a single-mode diamond waveguide with an indistinguishability of 63(9)% and a single-photon purity of $99.7^{+0.3}_{-2.5}$%. This is achieved by realizing coherent control of the optical transition of the SnV center with a π-rotation fidelity of 77.1(8)% realized in 1.71(1) ns. Thus, we show that the SnV center has sufficient photonic coherence to satisfy the requirements for quantum networking.

We perform our experiments on a diamond grown via chemical vapor deposition that has been implanted with Sn^{++} ions (350 keV; 7^o implantation angle; 10^9 cm^{-2} fluence), annealed, and subsequently fabricated into a diamond waveguide chiplet [36, 37]. A chiplet consists of eight single-mode waveguides, each 50 μm long with a rectangular cross-section of 200 nm by 270 nm. Figure 1(a) shows a characteristic device. The waveguides have an adiabatic taper over a distance of 9 μm at their two ends. This geometry is chosen to maximize the SnV center's emission out-coupling efficiency in finite-difference-time-domain simulations [37]. A support diamond structure connects the waveguides and provides sufficient structural integrity to allow the chiplet to be pick-and-placed onto the edge of a silicon substrate [31]. Such placement allows the light emitted by the SnV center to be collected by a single-mode lensed fiber giving a 23(3)-fold enhancement in collection efficiency relative to conventional confocal microscopy for the emitter studied in this work [37].

As indicated in Fig. 1(b), the excitation and collection modes are decoupled through orthogonal propagation di-

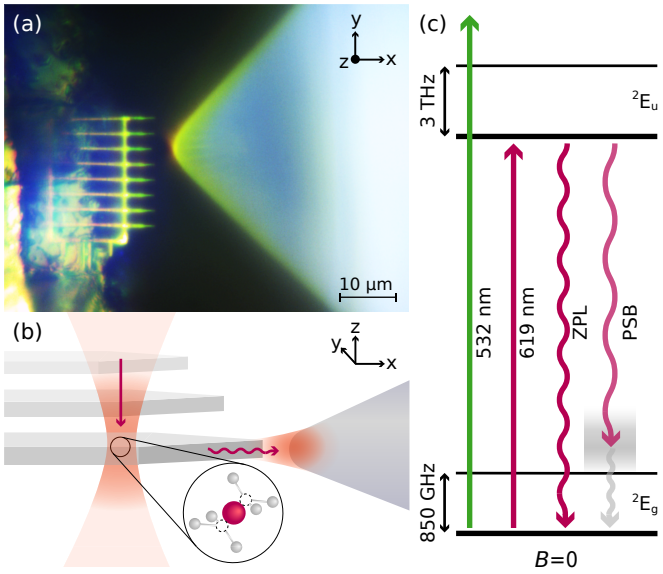

FIG. 1. (a) Microscope photograph of the waveguide to lensed fiber alignment. The waveguide array is placed on the edge of a silicon substrate such that it protrudes over the edge. A 3-axis nanopositioning stack is used to align a lensed fiber to a single waveguide. (b) Diagrammatic representation of the excitation and collection scheme. The SnV center is excited orthogonally to the waveguide axis but fluorescence is collected through the lensed fiber. (c) Electronic structure of the tin-vacancy center with no magnetic field. Off-resonant 532-nm and on-resonance 619-nm lasers are employed throughout this work to generate emission into the ZPL and PSB radiative decay pathways.

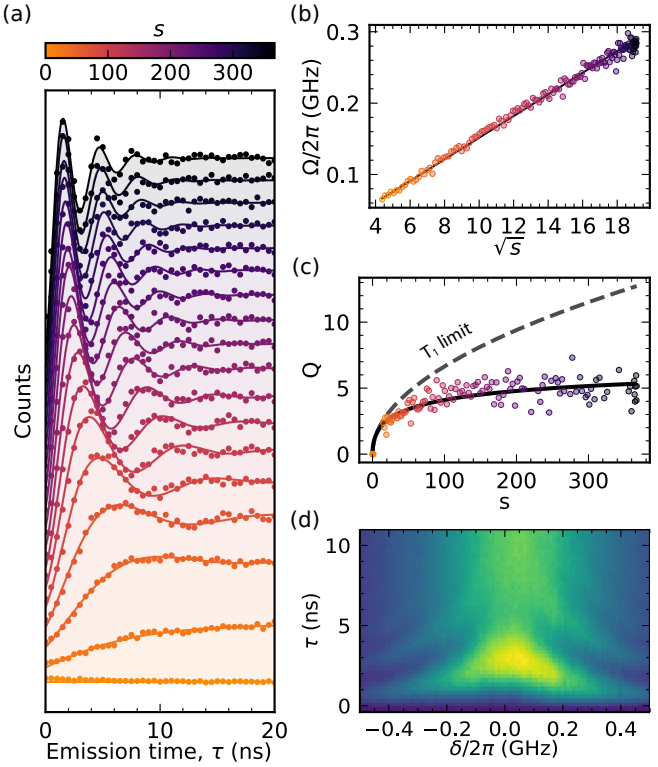

FIG. 2. (a) Histogrammed PSB fluorescence during a 20-ns-long resonant laser pulse. Curves are shown in a linear scale as a function of the saturation parameter, s. Solid curves correspond to individual fits to a master equation described in the main text [37]. At the highest saturation parameter the excited-state population saturates to 0.5 at long times. (b) Optical Rabi frequency Ω extracted from panel a as a function of $\sqrt{s}$. The black line is a linear fit with zero intercept. (c) Quality factor Q of the Rabi oscillation as a function of s. The solid black curve is a fit to a master-equation including a pure dephasing rate proportional to Ω. The dashed black curve shows the absolute coherence limit. (d) Detuning (δ) dependence of the Rabi oscillations at $s = 102(4)$ for the same excitation scheme as panel a. PSB fluorescence is color-coded with blue (yellow) corresponding to low (high) fluorescence.

rections. In this geometry, we achieve a continuous-wave laser suppression in excess of 60 dB. The SnV fluorescence collected through the lensed fiber is then routed from inside the cryostat, held at a temperature of 3.6 K, to our optical setup [37].

In the absence of magnetic field, the SnV center has a spin-degenerate optical transition between the lower orbital branch of the ground state and the lower orbital branch of the excited state [38]. To address this transition resonantly, we employ a 619-nm laser, as highlighted in Fig. 1(c). Also highlighted are the two radiative-decay pathways, the zero-phonon line (ZPL) and phonon sideband (PSB). This resonant drive induces occasional blinking of the SnV center. To remedy this we alternate between resonant and off-resonant 532-nm excitation [37], which pumps the emitter into the required, photo-active, -1 charge state [35]. The studied emitter has an excited-state lifetime T_1 of 7.44(20) ns, as measured through pulsed excitation, which corresponds to a transform-limited linewidth $\Gamma_0/2\pi$ of 21.4(2) MHz [37]. This is longer than the 4.5 ns reported for bulk diamond [34], likely due to the emitter being positioned close to the diamond-air interface [22, 39].

We first demonstrate optical control of the SnV center through resonant excitation and collection of the PSB. Figure 2(a) shows the averaged PSB fluorescence during a fixed-length 20-ns-long resonant 619-nm pulse starting at time $\tau = 0$. The histogrammed time-resolved fluorescence throughout the pulse is proportional to the instantaneous excited-state population and shows Rabi oscillations between the ground and excited state levels. The laser power P is parameterized by the saturation parameter $s = P/P_{\text{sat}}$, where $P_{\text{sat}} = 31(2)$ nW is the resonant laser power at which the Rabi rate Ω equals $\Gamma_0/\sqrt{2}$. For each power the excited-state population is fit to a two-level master equation, from which we extract the corresponding Ω and dephasing rate [37, 40, 41]. At the highest driving power ($s = 367(1)$), it takes 1.71(1) ns to perform an optical π-rotation, much faster than the lifetime (T_1) of the emitter, with an extracted fidelity of 77.1(8)%.

To investigate the effects of decoherence, the master equation used to fit Fig. 2(a) includes spontaneous emis-

sion and pure dephasing, as well as a shot-to-shot detuning fluctuation resulting in inhomogeneous dephasing [37]. We confirm in Fig. 2(b) a direct proportionality of the Rabi rate on the square root of the saturation parameter through the relationship $\Omega = \Gamma_0\sqrt{s/2}$. This linear relationship extends to our highest probed s and indicates that control-limiting imperfections such as phonon-coupling or multi-level driving do not cause an appreciable deviation from the master-equation model [37]. Figure 2(c) shows the power dependence of the quality factor Q, defined as the product of Ω and the $1/e$ envelope decay time extracted from the master-equation fits. In the low excitation power regime, the quality factor increases with power and agrees with the limit set by the finite T_1 lifetime. At higher powers the quality factor saturates which implies a laser-induced dephasing mechanism best modeled with a rate that linearly depends on Ω [42].

By varying the frequency of the resonant laser, we also probe the dependence of the fluorescence on the detuning $\delta = \omega_l - \omega_0$, where ω_l and ω_0 are the angular frequencies of the 619-nm resonant laser and the transition, respectively. Figure 2(d) shows the time evolution of the fluorescence as a function of δ at $s = 102(4)$, yielding a Rabi rate of 153(3) MHz at $\delta = 0$ and faster, lower-amplitude, oscillations for $\delta \neq 0$. The ability to vary the detuning, phase and amplitude of the resonant laser pulses enables multi-axis control of the optical qubit [37, 42].

We next leverage multi-axis control to probe the coherence of the optical transition directly through pulsed resonant excitation. Figure 3(a) displays the measurements of Ramsey interferometry and Hahn-echo dynamical decoupling. We read out the state of the emitter by integrating the fluorescence after the final $\pi/2$-rotation. Varying the phase of this $\pi/2$-rotation provides the means to measure the population contrast between the ground and excited states [33, 42]. The solid teal curve in Fig. 3(a) is a fit to the Ramsey-interferometry data using the master-equation model employed previously [37]. This yields an inhomogeneous dephasing time T_2^* of 4.54(2) ns, corresponding to a shot-to-shot spectral drift of 82.6(5) MHz at full width at half maximum (FWHM). The Hahn-echo contrast decay envelope provides a measurement of the pure-dephasing rate Γ_{PD}. A fit to the raw contrast results in $\Gamma_{PD}/2\pi = 6.39(14)$ MHz and an inferred homogeneous linewidth of $\Gamma/2\pi = (\Gamma_0 + 2\Gamma_{PD})/2\pi = 34.8(7)$ MHz. This linewidth is only a factor of 1.63(4) from its intrinsic Fourier limit (Γ_0) despite the emitter's close proximity (< 60 nm) to nanostructured surfaces.

We next probe the spectral stability on longer timescales by observing the shot-to-shot variation of the transition frequency through fast photoluminescence excitation (PLE) scans at $s = 0.8(1)$. Each scan alternates between 500 ms of resonant 619-nm and off-resonant 532-nm excitation. During the resonant section, $\delta/2\pi$ is repeatedly scanned from -100 MHz to 100 MHz using 3-µs-long linearly-chirped laser pulses. Figure 3(b) shows

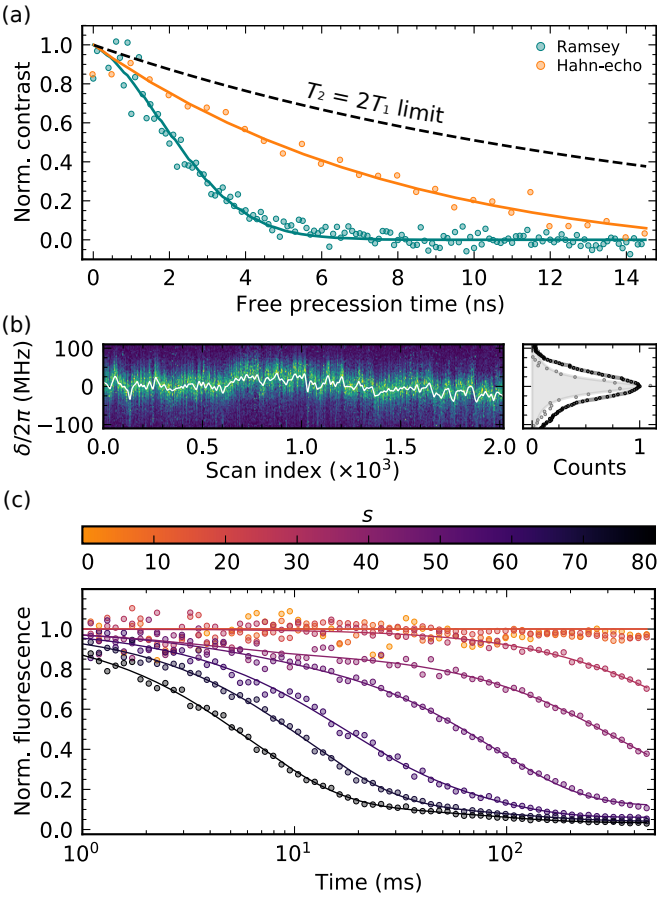

FIG. 3. (a) Ramsey (teal) and Hahn-echo (orange) contrast decay envelope measurements with master equation fits (solid curves) [37]. The dashed black curve shows the absolute coherence limit of $T_2 = 2T_1$. For visual clarity, the contrast at zero free-precession time is normalized to one. (b) Left: Shot-to-shot evolution of the PLE lineshape. Each vertical cut shows a histogram resulting from fast repeated PLE scans averaged over 500 ms. Off-resonant 532-nm excitation is applied between resonant sections. The solid white line follows the emitter's resonance frequency. Right: An example linecut (gray) and overall inhomogeneous distribution of all linecuts (black), with Lorentzian and Gaussian fits respectively. (c) Average PLE intensity as a function of time following a 532-nm off-resonant reset pulse for multiple saturation parameters. Solid curves are fits to bi-exponential decays.

the spectral evolution over 34 minutes. Within each vertical cut, and after correcting for power broadening, the linewidth is 35(10) MHz which is commensurate with the homogeneous linewidth inferred from the Hahn-echo measurement. This indicates that there are no significant, additional, dephasing mechanisms present between the tens of nanoseconds timescale probed in Fig. 3(a), and the 500-ms timescale probed by the PLE scans in Fig. 3(b).

Over multiple cuts, the central frequency, extracted from Lorentzian fits, does not show significant variation over consecutive scans. Over the entire measurement, the central frequency variation tends towards a normal

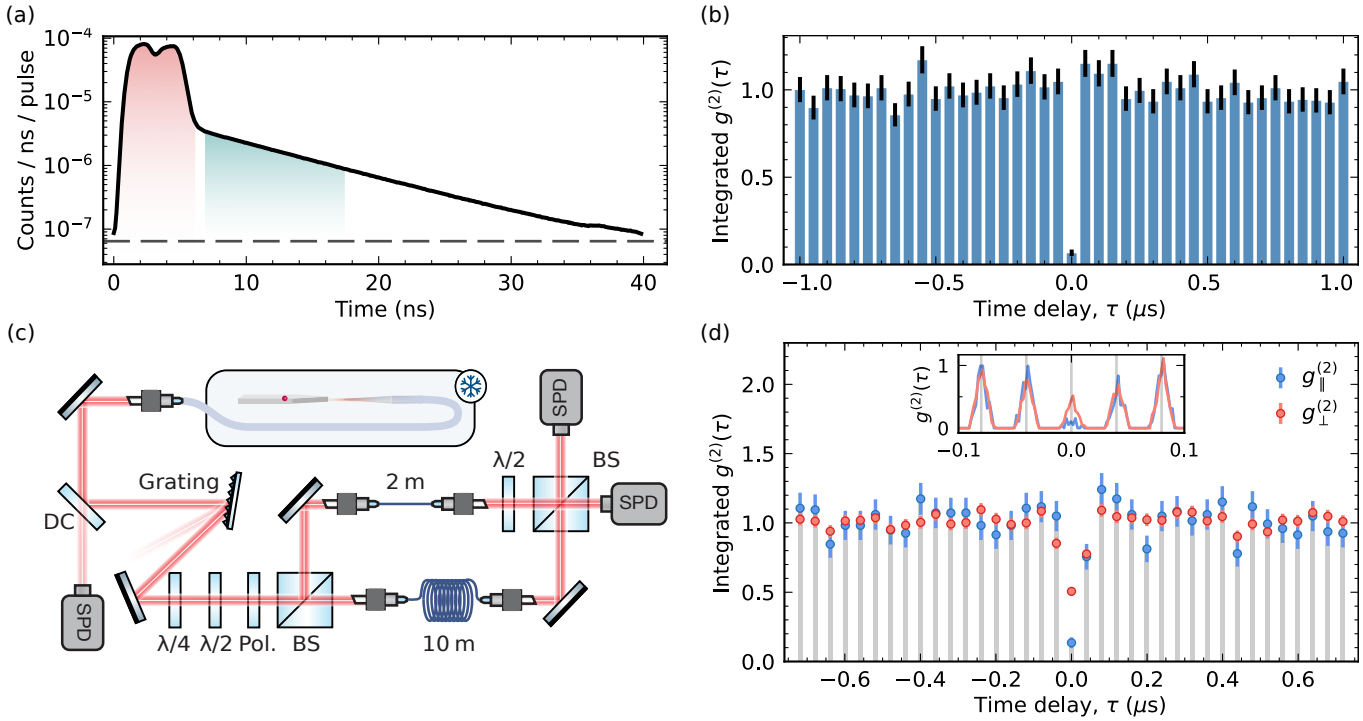

FIG. 4. (a) Time-resolved ZPL fluorescence under excitation with a 4-ns-long resonant laser pulse. Red and teal shadings correspond to the regions when the laser excitation is present and when the ZPL fluorescence is collected, respectively. The dashed line corresponds to the average background, as extracted from a far detuned ($\delta/2\pi$ = 6 GHz) laser pulse [37]. (b) Second-order autocorrelation of the ZPL fluorescence under pulsed resonant excitation. The recorded value $g^{(2)}(0)_{\mathrm{raw}} = 0.067(23)$ corresponds to a background-corrected photon purity of $99.7^{+0.3}_{-2.5}$%. (c) Experimental setup for the HOM measurement. Abbreviations: quarter-wave plate ($\lambda/4$), half-wave plate ($\lambda/2$), polarizer (Pol.), beamsplitter (BS) and dichroic mirror (DC). (d) Pulsed two-photon interference measurement for the parallel (blue) and perpendicular (red) polarization configurations, where the coincidence counts are integrated for each pulse. We extract a background-corrected photon indistinguishability of $V = 73(13)$% for photons collected within the teal region of panel a. Inset: time-resolved distribution of coincidences around $\tau = 0$.

distribution with a FWHM of 64(1) MHz. Such inhomogeneous broadening has been observed for the nitrogen-vacancy center [14], and more recently the SnV center [35], and is likely due to the off-resonant laser rearranging the local charge environment. For the nitrogen-vacancy center, the photo-induced spectral broadening can be over 0.5 GHz, or 35-times broader than the intrinsic linewidth [43]. In contrast, electric noise only detunes the SnV center through a second-order Stark shift [25] leading to a significantly narrower inhomogeneous linewidth. Figure 3(b) shows an inhomogeneous broadening of a factor of $\sim$ 2 compared to its homogeneous linewidth.

The 532-nm off-resonant excitation serves to photostabilize the emitter as resonant excitation pumps the emitter stochastically into a dark state [35]. To establish the timescale of this pumping, we monitor the decay of PLE intensity following a 532-nm off-resonant pulse. Repeatedly scanning 300 MHz across the transition makes the measurement insensitive to spectral diffusion. Figure 3(c) shows the decay of PSB fluorescence for various resonant excitation powers. The solid curves in Fig. 3(c) are fits to a bi-exponential model [44], where the dominant component reveals the time scale of pumping into the dark state. At the highest laser power, fluorescence persists over milliseconds allowing an average of $\sim 10^6$ π-pulses to be applied before pumping into the dark state. When considered in concert with Fig. 3(b), our emitter remains spectrally stable and optically active on a many millisecond timescale as required for quantum networking [45].

To probe the indistinguishability of the emitted photons, we isolate the ZPL using spectral filtering. We employ two electro-optic modulators for fast optical pulsing of the resonant excitation laser and time-tag the ZPL fluorescence. This reduces the background from laser scattering in excess of 30 dB, which combined with the orthogonal excitation and collection directions results in a total laser suppression greater than 90 dB. Figure 4(a) shows the time-resolved ZPL fluorescence after a 4-ns-long resonant excitation pulse. The large laser suppression yields a signal-to-background ratio of 23.91(3) during the first 11.1 ns following the excitation pulse, which corresponds to 80(1)% of the integrated ZPL fluorescence [37].

Routing the ZPL emission through a Hanbury-Brown

and Twiss interferometer [46], we measure a zero-delay second-order intensity correlation $g^{(2)}(0)_{\mathrm{raw}}$ of 0.067(23), as shown in Fig. 4(b). This is comparable to previous reports where only the PSB was collected, despite the added technical challenge of resonant collection in this work [33, 34]. Correcting for our detector dark-count rates, we calculate a background-corrected photon purity $(1 - g^{(2)}(0))$ of $99.7^{+0.3}_{-2.5}\%$.

Figure 4(c) shows our HOM-interferometry setup [37]. Before the interferometer, we employ a dichroic mirror and a grating to filter photons within a 245(6) GHz bandwidth (FWHM) centered on the ZPL transition. This filtered emission is routed through polarization control optics and into the interferometer with a relative time delay Δt of 39.93(2) ns between the two arms. To ensure temporal overlap between subsequently emitted photons we apply laser pulses with a repetition period matching Δt. A half-wave plate placed in the short-arm of the interferometer controls the relative polarization between the two interfering photons.

Figure 4(d) shows the second-order intensity correlation measured across the two output ports of the interferometer for ZPL fluorescence integrated over the first 11.1 ns after the excitation pulse. When the polarizations of two interferring photons are orthogonal to each other, we measure $g^{(2)}_{\perp}(0) = 0.51(3)$, in agreement with the theoretically expected value of 0.5. When the polarizations of the photons are matched, we measure $g^{(2)}_{\parallel}(0) = 0.22(3)$. The raw visibility, $V_{\mathrm{raw}} = 1 - g^{(2)}_{\parallel}(0)/g^{(2)}_{\perp}(0) = 56(8)\%$, is a measurement of the indistinguishability of the emitted photons. Correcting for the background and finite classical interferometric contrast, we calculate a photon indistinguishability V of 73(13)%. When the time window is extended to the full decay observed in Fig 4(a) the indistinguishability is reduced to $V = 63(9)\%$ [37].

We compare our measured indistinguishability to a model that includes homogeneous broadening as the source of photon distinguishability. Given the measured Γ_{PD}, we compute an expected HOM visibility V_{sim} of 63.2(4)% in agreement with our measured value [37]. Considering the slow spectral diffusion measured in Fig 3(b), the HOM visibility measured here should extend to interferometer delays greater than 100 ms.

In this work, we demonstrate coherent control of the optical transition of the SnV in diamond. We achieve a π-pulse time of 1.71(1) ns and two-photon quantum interference of resonant photons with an indistinguishability of 63(9)%. Purcell enhancement of the emitter, such as through optical microcavities [47] or photonic crystal cavities [28–30], increases the radiative decay rate and thus reduces the sensitivity to dephasing. An overall Purcell enhancement factor of 12, already achieved using SnV centers in nanocavities [29, 30], would yield a photon indistinguishability in excess of 95%. Moreover, fabrication and material processing improvements, known to result in improved optical quality of SnV centers in bulk diamond [22], should enhance the optical coherence. These advancements provide a feasible route to near-unity photon indistinguishability in the near-term.

Using the two-photon interference presented in this work, in combination with control of the spin degree of freedom [33], one could realize spin-photon entanglement [5, 48, 49] and entanglement of remote emitters [4, 50, 51]. Modest improvements in the indistinguishability of the photons would position multi-photon entangled states as the next achievement using the SnV center [52, 53].

ACKNOWLEDGMENTS

We acknowledge support from the ERC Advanced Grant PEDESTAL (884745), the EU Quantum Flagship 2D-SIPC. J.A.M. acknowledges support from the Winton Programme and EPSRC DTP, R.A.P. from the General Sir John Monash Foundation, K.C.C. from the National Science Foundation Graduate Research Fellowships Program (GRFP) and the NSF STC Center for Integrated Quantum Materials (CIQM), NSF Grant No. DMR-1231319 and NSF Award No. 1839155, C.P.M. from the EPSRC DTP, A.M.S. from EPSRC/NQIT, R.D. from the Gates Cambridge Trust, M.T. from the Army Research Laboratory ENIAC Distinguished Postdoctoral Fellowship, and D.A.G. from a St John's College Title A Fellowship and a Royal Society University Research Fellowship. D.E. acknowledges further support by the MITRE Quantum Moonshot Program.

* These authors contributed equally to this work.

† Correspondence should be addressed to: dorian.gangloff@eng.ox.ac.uk, englund@mit.edu, ma424@cam.ac.uk.

[1] S. D. Barrett and P. Kok, Efficient high-fidelity quantum computation using matter qubits and linear optics, Physical Review A **71**, 060310 (2005).

[2] B. Lanyon, P. Jurcevic, M. Zwerger, C. Hempel, E. Martinez, W. Dür, H. Briegel, R. Blatt, and C. F. Roos, Measurement-based quantum computation with trapped ions, Physical Review Letters **111**, 210501 (2013).

[3] H. Wang, J. Qin, X. Ding, M.-C. Chen, S. Chen, X. You, Y.-M. He, X. Jiang, L. You, Z. Wang, *et al.*, Boson sampling with 20 input photons and a 60-mode interferometer in a 1 0 14-dimensional hilbert space, Physical Review Letters **123**, 250503 (2019).

[4] C. Cabrillo, J. I. Cirac, P. Garcia-Fernandez, and P. Zoller, Creation of entangled states of distant atoms by interference, Physical Review A **59**, 1025 (1999).

[5] R. Vasconcelos, S. Reisenbauer, C. Salter, G. Wachter, D. Wirtitsch, J. Schmiedmayer, P. Walther, and M. Trupke, Scalable spin–photon entanglement by time-

to-polarization conversion, npj Quantum Information **6**, 1 (2020).
[6] H. Bernien, B. Hensen, W. Pfaff, G. Koolstra, M. S. Blok, L. Robledo, T. H. Taminiau, M. Markham, D. J. Twitchen, L. Childress, *et al.*, Heralded entanglement between solid-state qubits separated by three metres, Nature **497**, 86 (2013).
[7] Z.-S. Yuan, Y.-A. Chen, B. Zhao, S. Chen, J. Schmiedmayer, and J.-W. Pan, Experimental demonstration of a bdcz quantum repeater node, Nature **454**, 1098 (2008).
[8] K. Azuma, K. Tamaki, and H.-K. Lo, All-photonic quantum repeaters, Nature Communications **6**, 1 (2015).
[9] Z.-D. Li, R. Zhang, X.-F. Yin, L.-Z. Liu, Y. Hu, Y.-Q. Fang, Y.-Y. Fei, X. Jiang, J. Zhang, L. Li, *et al.*, Experimental quantum repeater without quantum memory, Nature photonics **13**, 644 (2019).
[10] D. Lago-Rivera, S. Grandi, J. V. Rakonjac, A. Seri, and H. de Riedmatten, Telecom-heralded entanglement between multimode solid-state quantum memories, Nature **594**, 37 (2021).
[11] C.-K. Hong, Z.-Y. Ou, and L. Mandel, Measurement of subpicosecond time intervals between two photons by interference, Physical Review Letters **59**, 2044 (1987).
[12] M. Zwerger, H. Briegel, and W. Dür, Measurement-based quantum communication, Applied Physics B **122**, 1 (2016).
[13] T. Rudolph, Why i am optimistic about the silicon-photonic route to quantum computing, APL Photonics **2**, 030901 (2017).
[14] H. Bernien, L. Childress, L. Robledo, M. Markham, D. Twitchen, and R. Hanson, Two-photon quantum interference from separate nitrogen vacancy centers in diamond, Physical Review Letters **108**, 043604 (2012).
[15] A. Sipahigil, K. D. Jahnke, L. J. Rogers, T. Teraji, J. Isoya, A. S. Zibrov, F. Jelezko, and M. D. Lukin, Indistinguishable photons from separated silicon-vacancy centers in diamond, Physical Review Letters **113**, 113602 (2014).
[16] D. Chen, J. E. Froch, S. Ru, H. Cai, N. Wang, G. Adamo, J. Scott, F. Li, N. Zheludev, I. Aharonovich, *et al.*, Quantum interference of resonance fluorescence from germanium-vacancy color centers in diamond, Nano Letters **22**, 6306 (2022).
[17] N. Morioka, C. Babin, R. Nagy, I. Gediz, E. Hesselmeier, D. Liu, M. Joliffe, M. Niethammer, D. Dasari, V. Vorobyov, *et al.*, Spin-controlled generation of indistinguishable and distinguishable photons from silicon vacancy centres in silicon carbide, Nature Communications **11**, 1 (2020).
[18] C. Santori, D. Fattal, J. Vučković, G. S. Solomon, and Y. Yamamoto, Indistinguishable photons from a single-photon device, Nature **419**, 594 (2002).
[19] E. Neu, M. Fischer, S. Gsell, M. Schreck, and C. Becher, Fluorescence and polarization spectroscopy of single silicon vacancy centers in heteroepitaxial nanodiamonds on iridium, Physical Review B **84**, 205211 (2011).
[20] Y. N. Palyanov, I. N. Kupriyanov, Y. M. Borzdov, and N. V. Surovtsev, Germanium: a new catalyst for diamond synthesis and a new optically active impurity in diamond, Sci. Rep. **5**, 14789 (2015).
[21] M. K. Bhaskar, D. D. Sukachev, A. Sipahigil, R. E. Evans, M. J. Burek, C. T. Nguyen, L. J. Rogers, P. Siyushev, M. H. Metsch, H. Park, *et al.*, Quantum nonlinear optics with a germanium-vacancy color center in a nanoscale diamond waveguide, Phys. Rev. Lett. **118**, 223603 (2017).
[22] J. Görlitz, D. Herrmann, G. Thiering, P. Fuchs, M. Gandil, T. Iwasaki, T. Taniguchi, M. Kieschnick, J. Meijer, M. Hatano, *et al.*, Spectroscopic investigations of negatively charged tin-vacancy centres in diamond, New Journal of Physics **22**, 013048 (2020).
[23] D. D. Sukachev, A. Sipahigil, C. T. Nguyen, M. K. Bhaskar, R. E. Evans, F. Jelezko, and M. D. Lukin, Silicon-Vacancy Spin Qubit in Diamond: A Quantum Memory Exceeding 10 ms with Single-Shot State Readout, Physical Review Letters **119**, 223602 (2017).
[24] T. Iwasaki, Y. Miyamoto, T. Taniguchi, P. Siyushev, M. H. Metsch, F. Jelezko, and M. Hatano, Tin-vacancy quantum emitters in diamond, Physical Review Letters **119**, 253601 (2017).
[25] L. De Santis, M. E. Trusheim, K. C. Chen, and D. R. Englund, Investigation of the stark effect on a centrosymmetric quantum emitter in diamond, Physical Review Letters **127**, 147402 (2021).
[26] G. Thiering and A. Gali, Ab initio magneto-optical spectrum of group-iv vacancy color centers in diamond, Physical Review X **8**, 021063 (2018).
[27] E. N. Knall, C. M. Knaut, R. Bekenstein, D. R. Assumpcao, P. L. Stroganov, W. Gong, Y. Q. Huan, P.-J. Stas, B. Machielse, M. Chalupnik, *et al.*, Efficient source of shaped single photons based on an integrated diamond nanophotonic system, arXiv preprint arXiv:2201.02731 (2022).
[28] M. K. Bhaskar, R. Riedinger, B. Machielse, D. S. Levonian, C. T. Nguyen, E. N. Knall, H. Park, D. Englund, M. Lončar, D. D. Sukachev, *et al.*, Experimental demonstration of memory-enhanced quantum communication, Nature **580**, 60 (2020).
[29] A. E. Rugar, S. Aghaeimeibodi, D. Riedel, C. Dory, H. Lu, P. J. McQuade, Z.-X. Shen, N. A. Melosh, and J. Vučković, Quantum photonic interface for tin-vacancy centers in diamond, Physical Review X **11**, 031021 (2021).
[30] K. Kuruma, B. Pingault, C. Chia, D. Renaud, P. Hoffmann, S. Iwamoto, C. Ronning, and M. Lončar, Coupling of a single tin-vacancy center to a photonic crystal cavity in diamond, Applied Physics Letters **118**, 230601 (2021).
[31] N. H. Wan, T.-J. Lu, K. C. Chen, M. P. Walsh, M. E. Trusheim, L. De Santis, E. A. Bersin, I. B. Harris, S. L. Mouradian, I. R. Christen, *et al.*, Large-scale integration of artificial atoms in hybrid photonic circuits, Nature **583**, 226 (2020).
[32] C. Bradac, W. Gao, J. Forneris, M. E. Trusheim, and I. Aharonovich, Quantum nanophotonics with group iv defects in diamond, Nature Communications **10**, 1 (2019).
[33] R. Debroux, C. P. Michaels, C. M. Purser, N. Wan, M. E. Trusheim, J. A. Martínez, R. A. Parker, A. M. Stramma, K. C. Chen, L. de Santis, *et al.*, Quantum control of the tin-vacancy spin qubit in diamond, Physical Review X **11**, 041041 (2021).
[34] M. E. Trusheim, B. Pingault, N. H. Wan, M. Gündoğan, L. De Santis, R. Debroux, D. Gangloff, C. Purser, K. C. Chen, M. Walsh, *et al.*, Transform-limited photons from a coherent tin-vacancy spin in diamond, Physical Review Letters **124**, 023602 (2020).
[35] J. Görlitz, D. Herrmann, P. Fuchs, T. Iwasaki, T. Taniguchi, D. Rogalla, D. Hardeman, P.-O. Colard,

M. Markham, M. Hatano, *et al.*, Coherence of a charge stabilised tin-vacancy spin in diamond, npj Quantum Information **8**, 1 (2022).

[36] S. Mouradian, N. H. Wan, T. Schröder, and D. Englund, Rectangular photonic crystal nanobeam cavities in bulk diamond, Applied Physics Letters **111**, 021103 (2017).

[37] See Supplemental Material at [URL will be inserted by publisher] for information on experimental methods, theoretical simulations and extended data analysis, which includes references 38 to 51.

[38] C. Hepp, T. Müller, V. Waselowski, J. N. Becker, B. Pingault, H. Sternschulte, D. Steinmüller-Nethl, A. Gali, J. R. Maze, M. Atatüre, *et al.*, Electronic structure of the silicon vacancy color center in diamond, Physical Review Letters **112**, 036405 (2014).

[39] D. Jalas, K. M. Schulz, A. Y. Petrov, and M. Eich, Emission enhancement in dielectric nanocomposites, Optics Express **26**, 16352 (2018).

[40] V. Gorini, A. Kossakowski, and E. C. G. Sudarshan, Completely positive dynamical semigroups of n-level systems, Journal of Mathematical Physics **17**, 821 (1976).

[41] G. Lindblad, On the generators of quantum dynamical semigroups, Communications in Mathematical Physics **48**, 119 (1976).

[42] J. Bodey, R. Stockill, E. Denning, D. Gangloff, G. Éthier-Majcher, D. Jackson, E. Clarke, M. Hugues, C. L. Gall, and M. Atatüre, Optical spin locking of a solid-state qubit, npj Quantum Information **5**, 1 (2019).

[43] P. Siyushev, H. Pinto, M. Vörös, A. Gali, F. Jelezko, and J. Wrachtrup, Optically controlled switching of the charge state of a single nitrogen-vacancy center in diamond at cryogenic temperatures, Physical review letters **110**, 167402 (2013).

[44] R. Parker, N. Dontschuk, S.-I. Sato, C.-K. Lew, P. Reineck, A. Nadarajah, T. Ohshima, B. Gibson, S. Castelletto, J. McCallum, *et al.*, Infrared erbium photoluminescence enhancement in silicon carbide nano-pillars, Journal of Applied Physics **130**, 145101 (2021).

[45] M. Pompili, S. L. Hermans, S. Baier, H. K. Beukers, P. C. Humphreys, R. N. Schouten, R. F. Vermeulen, M. J. Tiggelman, L. dos Santos Martins, B. Dirkse, *et al.*, Realization of a multinode quantum network of remote solid-state qubits, Science **372**, 259 (2021).

[46] R. Brown and R. Q. Twiss, Correlation between photons in two coherent beams of light, Nature **177**, 27 (1956).

[47] D. Riedel, I. Söllner, B. J. Shields, S. Starosielec, P. Appel, E. Neu, P. Maletinsky, and R. J. Warburton, Deterministic enhancement of coherent photon generation from a nitrogen-vacancy center in ultrapure diamond, Physical Review X **7**, 031040 (2017).

[48] E. Togan, Y. Chu, A. S. Trifonov, L. Jiang, J. Maze, L. Childress, M. G. Dutt, A. S. Sørensen, P. R. Hemmer, A. S. Zibrov, *et al.*, Quantum entanglement between an optical photon and a solid-state spin qubit, Nature **466**, 730 (2010).

[49] W. Gao, P. Fallahi, E. Togan, J. Miguel-Sánchez, and A. Imamoglu, Observation of entanglement between a quantum dot spin and a single photon, Nature **491**, 426 (2012).

[50] P. C. Humphreys, N. Kalb, J. P. Morits, R. N. Schouten, R. F. Vermeulen, D. J. Twitchen, M. Markham, and R. Hanson, Deterministic delivery of remote entanglement on a quantum network, Nature **558**, 268 (2018).

[51] R. Stockill, M. Stanley, L. Huthmacher, E. Clarke, M. Hugues, A. Miller, C. Matthiesen, C. Le Gall, and M. Atatüre, Phase-tuned entangled state generation between distant spin qubits, Physical Review Letters **119**, 010503 (2017).

[52] D. Buterakos, E. Barnes, and S. E. Economou, Deterministic generation of all-photonic quantum repeaters from solid-state emitters, Physical Review X **7**, 041023 (2017).

[53] C. P. Michaels, J. A. Martínez, R. Debroux, R. A. Parker, A. M. Stramma, L. I. Huber, C. M. Purser, M. Atatüre, and D. A. Gangloff, Multidimensional cluster states using a single spin-photon interface coupled strongly to an intrinsic nuclear register, Quantum **5**, 565 (2021).